10
Planetary Rings

Hast any philosophy in thee, shepherd?

William Shakespeare, *As You Like It, III, ii*

10.1 Introduction

The first ring system to be observed in the solar system was discovered around Saturn by Galileo in 1610. Unsure of the nature of the phenomenon he had observed, he originally interpreted the ring ansae as two moons, one on each side of the planet. In a Latin anagram sent to fellow scientists he announced, *"I have observed the most distant planet to have a triple form"*. Galileo was surprised to find that the phenomenon had disappeared by 1612, only to reappear again soon afterwards. Huygens (1659) correctly attributed the varying appearance as being due to the different views of a thin disk of material surrounding Saturn. It was Maxwell (1859) who provided a mathematical proof that the rings could not be solid; they had to be composed of individual particles orbiting the planet.

The rings of Uranus were detected serendipitously in March 1977 by astronomers observing an occultation of a star by the planet. The *Voyager* spacecraft detected a faint ring around Jupiter (Smith et al. 1979a), and occultations of stars by Neptune led to the discovery of the ring arcs of Neptune, subsequently shown to be the optically thicker parts of a faint ring system. The flybys of the outer planets by the *Voyager* spacecraft and the continuing ground- and space-based observations of the ring systems have provided evidence of a wide variety of dynamical phenomena, which provide an ideal testing ground for some of the concepts covered in this book.

In this chapter we do not attempt to give a complete summary of knowledge concerning planetary rings, nor even to provide a summary of the dynamics of

ring systems. Instead, we concentrate on those aspects of ring dynamics that illustrate resonant phenomena and can be understood using simple extensions of the methods already discussed in previous chapters. Therefore it is important to realise that many of the properties of planetary ring systems can only be understood by undertaking a fluid dynamical approach to the problem. The chapters in Greenberg & Brahic (1984) provide comprehensive surveys of the field in 1984; Nicholson & Dones (1991) give a more recent summary of ring observations and research.

10.2 Planetary Ring Systems

Data on planetary rings are given in Appendix A. The relative sizes and locations of the different systems are shown in Fig. 10.1 on a uniform scale of planetary radii, following the example of Nicholson & Dones (1991). Figure 10.1 also shows the radial locations of the satellites that orbit in the vicinity of the rings. The synchronous orbit for each planet (dashed line) is dynamically important since under tidal forces all prograde satellites orbiting beyond it would move away from the planet and those orbiting inside it would approach the planet and eventually break up. Representative *Voyager* images of the ring systems of the outer planets are shown in Fig. 10.2.
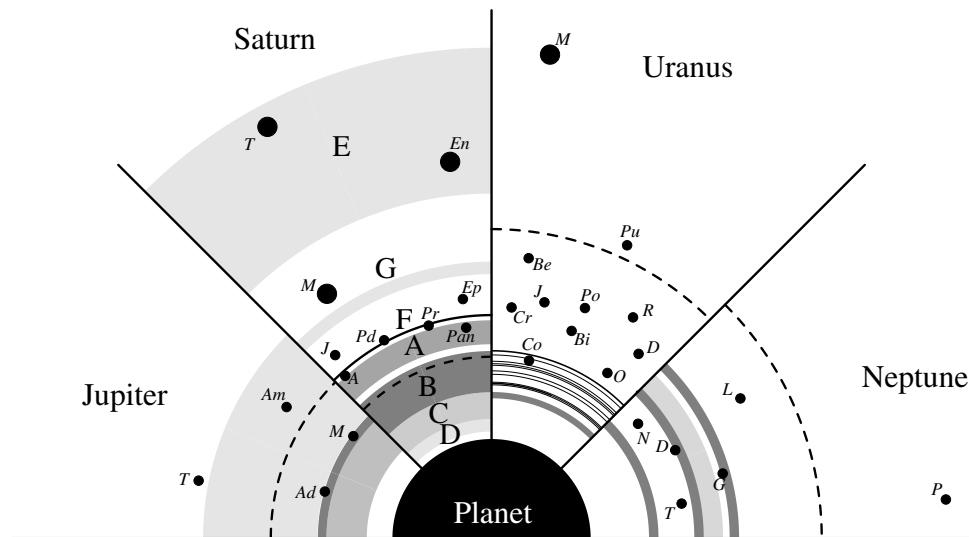

Fig. 10.1.   The ring systems of the outer planets and their accompanying satellites on a uniform scale of planetary radii. The location of the synchronous orbit for each planet is denoted by a dashed curve. (Adapted from Nicholson & Dones (1991).)
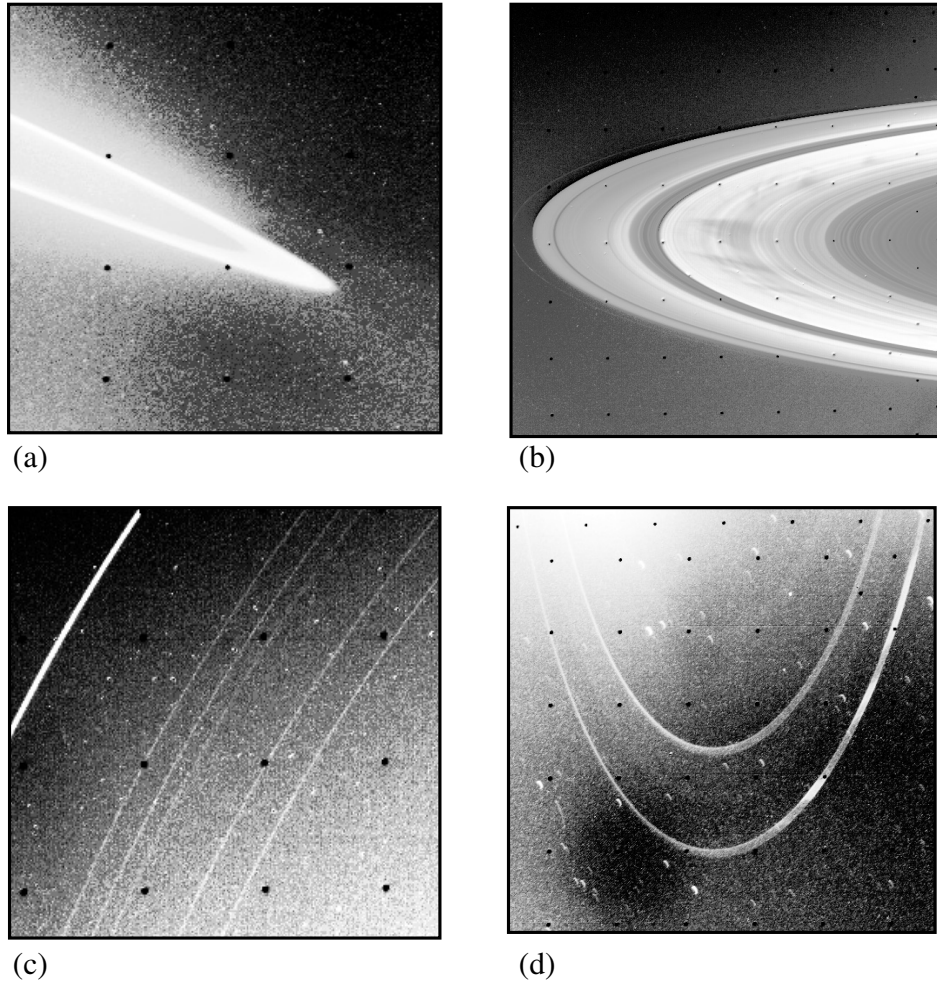
Fig. 10.2. Representative *Voyager* images of the ring systems of the outer planets: (a) Jupiter, showing the halo extending above the inner part of the main ring, (b) Saturn, showing the main rings (with "spokes"), (c) Uranus, showing six of the known narrow rings, and (d) Neptune, showing the azimuthal structure in the outermost ring. The scale in each image is different. *(Images courtesy of NASA/JPL.)*

10.2.1 The Rings of Jupiter

The optically thin (optical depth, $\tau < 3 \times 10^{-6}$) ring system of Jupiter was discovered by the *Voyager 1* spacecraft in March 1979 and further images were obtained by *Voyager 2* later that year (Smith et al. 1979a,b). The set of twenty-five Voyager images have been extensively analysed by Showalter (1985) and Showalter et al. (1987). The ring has also been detected from ground-based observations (Nicholson & Matthews 1991). The main ring, centred at 129,130 km, is $\sim$7,000 km wide with a sharp outer edge and a faint "gossamer" ring extending outwards beyond the orbit of Thebe. At the inner edge there is a toroidal-shaped halo of ring material, which is brighter close to the main ring and may extend more than halfway to the planet. The vertical structure extends

symmetrically for perhaps 10,000 km above and below the equatorial plane. A schematic representation of the ring system is shown in Fig. 10.3.

The optical forward-scattering properties of the ring are indicative of the presence of a large population of micron-sized particles. Dust in the jovian environment is subjected to significant nongravitational perturbations resulting in lifetimes of $\sim 10^{3\pm1}$ y, implying a readily available source of material (Burns et al. 1984). Two small satellites, Metis (radius ~ 20 km) and Adrastea (radius ~ 10 km), orbit in the outer part of the ring and it is the impact of meteoroids on these and other smaller objects that is thought to be the source of most of the ring material. Observations of the gossamer ring by the *Galileo* spacecraft show two separate bands of material, starting at the orbits of Thebe and Amalthea. The structure of these bands is strikingly similar to that detected in the zodiacal dust bands (see Fig. 7.17) and there is clear evidence that Thebe and Amalthea are the source objects for this jovian dust (Ockert-Bell *et al.* 1999, Burns *et al.* 1999).

Consolmagno (1983) and Burns et al. (1985) suggested that the Lorentz force experienced by a charged dust grain could help explain some of the structure of the jovian ring system. In particular, commensurate relationships between the
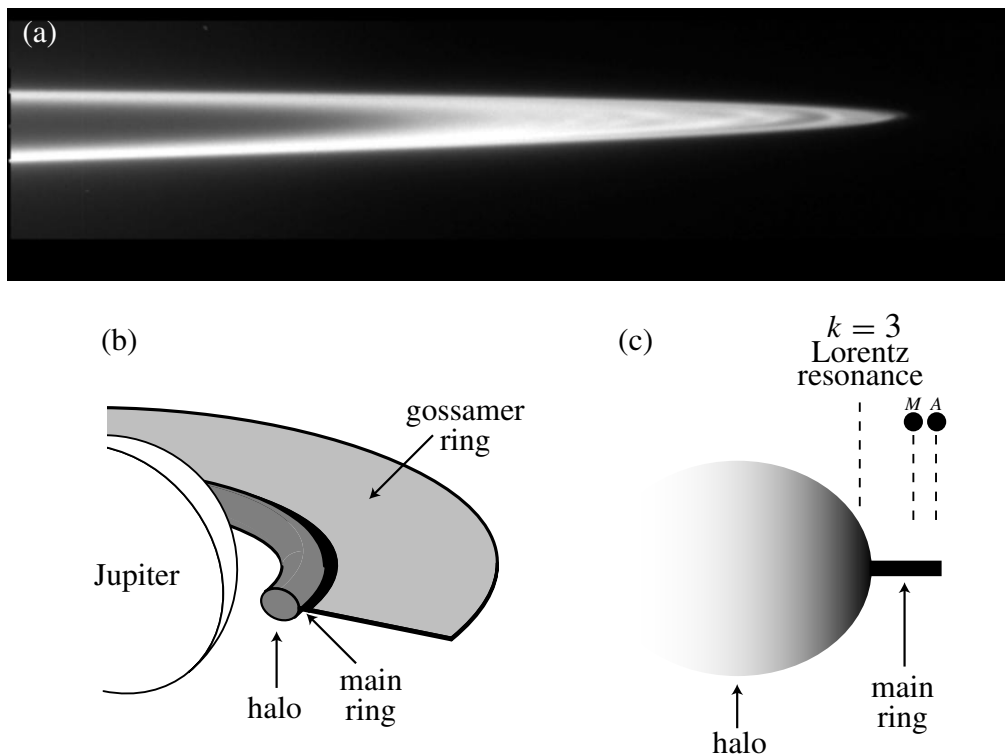

Fig. 10.3.   (a) A *Galileo* image of Jupiter's main ring *(image courtesy of NASA/JPL)*. A schematic illustration of the ring system showing (b) the main component with halo and gossamer ring and (c) the locations of Metis (M), Adrastea (A), and the suspected effect of the $k = 3$ Lorentz resonance at the inner edge of the main ring.

orbital period of the grain and the period of the electromagnetic force give rise to
the so-called Lorentz resonances (Burns et al. 1985), which occur at semi-major
axes given by

$$a_k = \left(\frac{k \mp 1}{k}\right)^{2/3} r_s, \qquad k = 1, 2, \ldots, \infty, \tag{10.1}$$

where r_s is the synchronous orbital radius. The $k = 3$ interior Lorentz resonance
occurs close to the transition point between the main ring and the halo (Schaffer
& Burns 1987).

10.2.2 The Rings of Saturn

The main ring system of Saturn (see Fig. 10.1 and Fig. 10.2b) consists of the
broad A and B rings separated by the Cassini division and the optically thin-
ner C and D rings. Exterior to the main rings lie the narrow, "braided" F ring
and the broader diffuse G and E rings. It is important to note that the main
ring system contains very few actual gaps; most of the ring features that appear
in the occultation profile (Fig. 10.4) are fluctuations in surface density. How-
ever, narrow gaps exist in the C ring, at the inner edge of the Cassini division,
and in the outer part of the A ring. Gaps in the C ring and Cassini division
are known to contain narrow, eccentric rings (Porco 1990), two of which are
thought to be subject to forced precession as a result of satellite resonances (Porco
1983, Nicholson & Porco 1988). This mechanism is discussed in Sect. 10.5.4
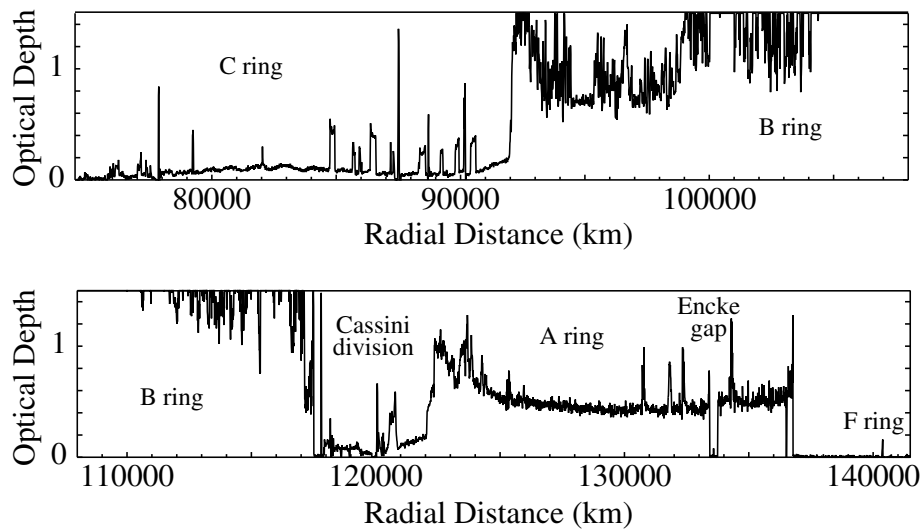below.

Fig. 10.4.   Optical depth profiles of the Saturn ring system obtained from the *Voyager*
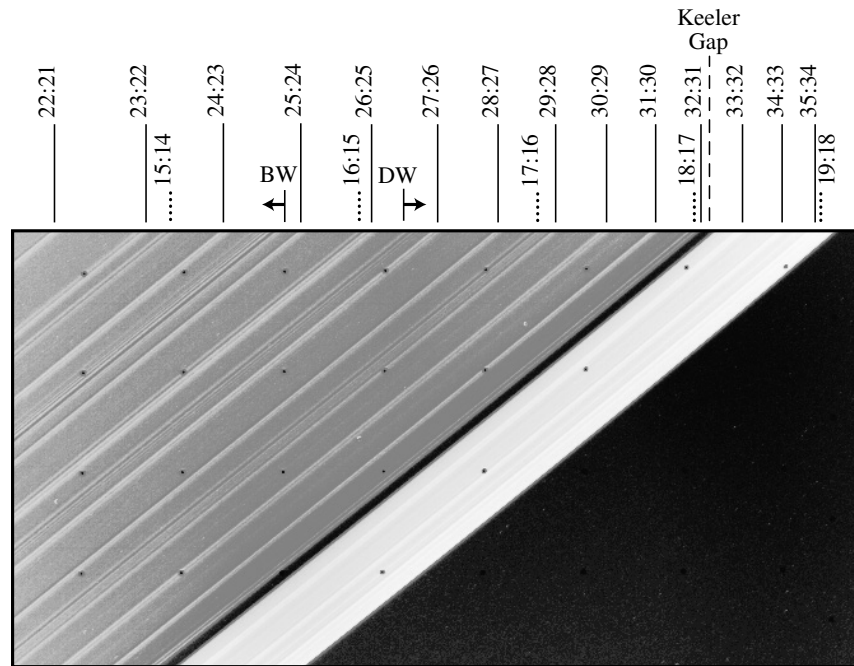photopolarimeter experiment (see Lane et al. 1982).

Fig. 10.5. The outer part of the A ring of Saturn showing the location of resonances with the F ring shepherding satellites Pandora (dotted lines) and Prometheus (solid lines). The locations and directions of propagation of a spiral bending wave (BW) and a spiral density wave (DW) associated with the Mimas 8:5 resonance are also indicated. *(Image courtesy of NASA/JPL.)*

Most of the structure in the A ring of Saturn seen in Fig. 10.4 can be explained by resonances with the smaller saturnian satellites. Figure 10.5 shows part of a *Voyager 2* image of the outer part of the A ring with annotation indicating the positions of all the resonances of the form $p + 1 : p$ with Pandora and Prometheus, which lie within the region. The ring features are caused by a succession of tightly wound, unresolved spiral density waves propagating away from the location of the resonances (see Sect. 10.4). There are also two features associated with the 8:5 resonance with Mimas. The outer one produces a spiral density wave propagating outwards and the inner one produces a spiral bending wave propagating inwards. Although the structure of the B ring is still poorly understood, there has been some progress in explaining some of the C ring structure in terms of resonances with planetary oscillations (Marley 1990, Marley & Porco 1993). Recently Hamilton & Burns (1994) have attempted to explain the properties of the extended E ring by including the effects of nongravitational forces on the micron-sized particles.

10.2.3 The Rings of Uranus

Prior to the *Voyager 2* encounter with Uranus in 1986, ground-based stellar occultation experiments had detected the presence of nine, narrow (typical widths
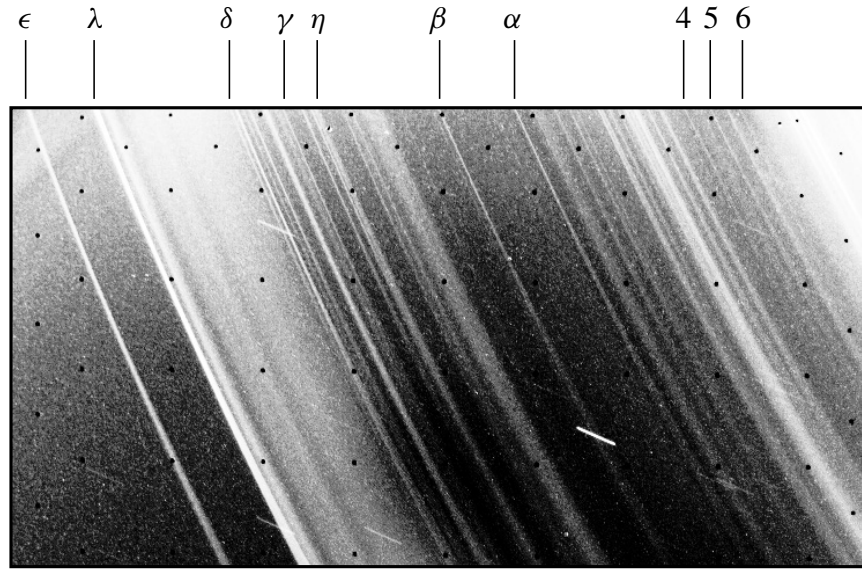
Fig. 10.6.   A *Voyager 2* image of the rings of Uranus in forward scattered light showing
the presence of numerous dust rings in addition to the nine rings detected from Earth-
based occultations. *(Image courtesy of NASA/JPL.)*

of $<$ 10 km) rings around the planet. *Voyager* images in back-scattered light
confirmed the existence of these rings as well as the λ ring orbiting between
the δ and ϵ rings and 1986U2R orbiting interior to ring 6. A 96 s exposure in
forward-scattered light revealed the presence of a large number of dust rings
(Fig. 10.6). French et al. (1991) provide a summary of the observations and
dynamical models of the uranian ring system.

The shepherding satellite model (Goldreich & Tremaine 1979a; see also
Sect. 10.5.3) for narrow rings has had considerable success in explaining the
confinement of the ϵ ring by the satellites Cordelia and Ophelia, which orbit in-
terior and exterior to the ring. Cordelia has a 24:25 outer eccentric resonance with
the inner edge of the ϵ ring and Ophelia has a 14:13 inner eccentric resonance at
the outer edge of the ring (Porco & Goldreich 1987). However, despite extensive
searches, no other satellites have been found in the main ring system, although
there is some evidence for their existence (see Murray & Thompson (1990)).

The ϵ ring is one of several in the uranian system to exhibit a variable width.
The occultation data demonstrate that each of these rings can be modelled by two
aligned ellipses of different semi-major axes and eccentricities, which precess
uniformly under the zonal gravity harmonics at a rate determined by the central
elliptical path. The two models proposed to explain this behaviour do not involve
the presence of unseen satellites. Instead they rely on either the self-gravity of the
ring (Goldreich & Tremaine 1979b) or the effectiveness of a "pinch" mechanism
(see Sect. 10.5.4) within the ring (Dermott & Murray 1980). The prediction of

a mean particle radius of 20–30 cm using the self-gravity model is in conflict with the *Voyager* observations of sizes > 70 cm.

10.2.4 The Rings of Neptune

Following the discovery of the rings of Uranus by ground-based, stellar occultation experiments in 1977, numerous attempts were made to discover a Neptunian ring system using similar methods. Hubbard et al. (1986) provided the first convincing evidence for the existence of ring material but only in $\sim 10\%$ of cases did such experiments yield any signatures, and in those a feature was detected on only one side of the planet. This led to the suggestion that Neptune had a system of "arcs" of ring material extending over $\sim 10°$ in longitude. The *Voyager 2* images (see, for example, Fig. 10.2d) show that Neptune has at least three, distinct rings (the Galle, Le Verrier, and Adams rings) and that the arcs are just the optically thicker parts ($\tau \approx 0.04$) of the outermost Adams ring (Smith et al. 1989). Additional rings include the Lassell ring extending outwards from the Le Verrier ring and bounded by the Arago ring and an unnamed ring that appears to share the same orbit as the moon Galatea. The three main arcs in the Adams ring were named Liberté, Egalité, and Fraternité, although it is now known that there are at least two more arcs, Egalité 2 and Courage, in the same ring (see the review article by Porco et al. 1995).

10.2.5 Rings and Satellites

It is clear from Fig. 10.1 that there is a close association between the location of ring systems and the orbits of small satellites. We know from our study of tidal evolution of satellites that objects in prograde orbits inside the synchronous orbit will evolve inwards due to the effect of the tides they raise on the planet. We also know that the Roche zone for each planet lies in the range of 1.44 to 2.24 planetary radii. Therefore we would expect satellites brought in under tidal effects to break up as they approach the planet. In such cases the satellites act as sources of ring material. However, the rings are also subject to the gravitational perturbations from the satellite remnants. These can have the effect of confining some rings while causing other ring material to be disrupted. These processes for narrow rings are discussed in Sect. 10.5 below. In all such cases it is important to recognise the role of resonance in determining ring structure.

10.3 Resonances in Rings

The close proximity of rings and satellites in each system (see Fig. 10.1) suggests that there could be significant mutual gravitational perturbations. In the case of Saturn's rings, for example, virtually all the structure in the A ring can be understood in the context of resonances between ring particles and the satellites

that orbit nearby (see Fig. 10.5). There are also resonant features in other ring systems. Therefore it is important to examine the nature of these resonant interactions in order to understand the observed features.

In Sect. 2.6 we showed that elliptical motion about a spherical central object can be considered in terms of motion around an epicentre which moves at a uniform rate equal to the mean motion n around the central object, provided the eccentricity of the orbit is small. The secondary object traces out a closed, centred ellipse about the guiding centre. In Sect. 6.11 we considered the case of an object orbiting an oblate planet with an axisymmetric potential. As well as the standard $1/r$ potential, the particle experiences the effect of the zonal harmonic coefficients J_2, J_4, etc. We showed that these terms cause the orbit to rotate in space, giving rise to three separate frequencies, n, κ, and ν (see Eqs. (6.244)–(6.246)). These quantities are the modified mean motion, the epicyclic frequency, and the vertical frequency, respectively.

Now consider the gravitational effect of a perturbing satellite with semi-major axis a'. The satellite will have its own set of frequencies n', κ', and ν' given by Eqs. (6.244)–(6.246) with a replaced by a'. The satellite's potential can be expanded in a Fourier series (see Chapter 6). For each argument in the expansion the *pattern speed,* Ω_p, is defined as the angular frequency of a reference frame in which this argument is stationary. This will depend on the exact combination of frequencies under consideration and may be written as

$$m\Omega_\mathrm{p} = mn' + k\kappa' + p\nu' \qquad (10.2)$$

or, because $\kappa' = n' - \dot\varpi'$ and $\nu' = n' - \dot\Omega'$,

$$m\Omega_\mathrm{p} = (m + k + p)n' - k\dot\varpi' - p\dot\Omega', \qquad (10.3)$$

where m, k, and p are integers and m is nonnegative. The strongest resonances occur when an integer multiple of the difference between n and Ω_p is equal to zero (for *corotation resonances*) or to the natural frequency of the radial or vertical oscillations of the ring particle (for *eccentric* (or *Lindblad*) *resonances* and *vertical resonances* respectively). The new terminology has its origins in galactic dynamics rather than solar system dynamics. We shall see, by means of specific examples, how these resonances are related to those described in Chapter 8. A summary of this work is given in Murray (1999).

10.3.1 Perturbations in Semi-major Axis and Corotation Resonances

A corotation resonance occurs where the pattern speed of the perturbing potential matches the orbital frequency of the particle. In this case

$$m(n - \Omega_\mathrm{p}) = 0. \qquad (10.4)$$

From the definition of Ω_p this implies that the resonance condition is

$$(m + k + p)n' - mn - k\dot\varpi' - p\dot\Omega' = 0. \qquad (10.5)$$

If we ignore the variation of the mean longitude at epoch, this in turn can be considered as setting the condition $\dot{\varphi}_{cr} = 0$, where φ_{cr} is the resonant angle given by

$$\varphi_{cr} = (m + k + p)\lambda' - m\lambda - k\varpi' - p\Omega'. \tag{10.6}$$

If we adopt our usual notation whereby the coefficient of λ' in the resonant angle is always j (see Chapter 6 and Appendix B) then

$$\varphi_{cr} = j\lambda' + (k + p - j)\lambda - k\varpi' - p\Omega', \tag{10.7}$$

where $j = m + k + p$. We can see that this argument satisfies the d'Alembert relation and we already know that for this to be a valid argument $|p|$ must be even; this is because the inclinations always occur in even powers and hence the sum of the coefficients of the nodes must always be even. Furthermore, this is the argument of a resonance of order $|k + p|$. The lowest order term associated with this resonant argument will be $\mathcal{O}(e'^{|k|} I'^{|p|})$ (see Sect. 6.7 and Appendix B). The 1:1 resonance (where $p = k = 0$) is clearly a special case of a corotation resonance.

Neither the longitude of pericentre nor the longitude of ascending node of the ring particle are involved in the resonant argument, φ_{cr}, of a corotation resonance. From Lagrange's equations this means that only the ring particle's semi-major axis is affected by a corotation resonance.

The relevant part of the disturbing function (cf. Eq. (8.26)) is

$$\mathcal{R} = \frac{\mathcal{G}m'}{a'} f_d(\alpha) e'^{|k|} s'^{|p|} \cos \varphi_{cr}, \tag{10.8}$$

where φ_{cr} is given in Eq. (10.7). The exact form of $f_d(\alpha)$ depends on the resonance in question (see Table 8.1). From the definition of the corotation resonance the resonant angle can be written as

$$\varphi_{cr} = -m(\lambda - \Omega_p t) + \text{constant}, \tag{10.9}$$

and therefore there are m equilibrium points in the frame rotating with the pattern speed Ω_p where libration is possible.

The geometry of a simple corotation resonance is shown in Fig. 10.7 for the case of a 3:2 resonance with $j = 3$, $m = 2$, $k = 1$, $p = 0$, and $e' = 0.25$. Because $m = 2$ there are two possible libration points in the frame rotating with the pattern speed of the perturbing satellite. In this frame the path of the satellite (the outer curve in Fig. 10.7) is closed (cf. Fig. 5.10 and Fig. 8.4c for the 2:3 resonance). Because the particle is close to but not at the exact resonance (i.e., it is not located at one of the two equilibrium points) it will librate about the equilibrium point. We have discussed this behaviour in Chapter 8.

We can calculate the maximum width of a corotation resonance by using the pendulum model developed in Chapter 8. For example, in the case of the 3:2 resonance discussed above we have $k = 1$ and $p = 0$, which corresponds to the
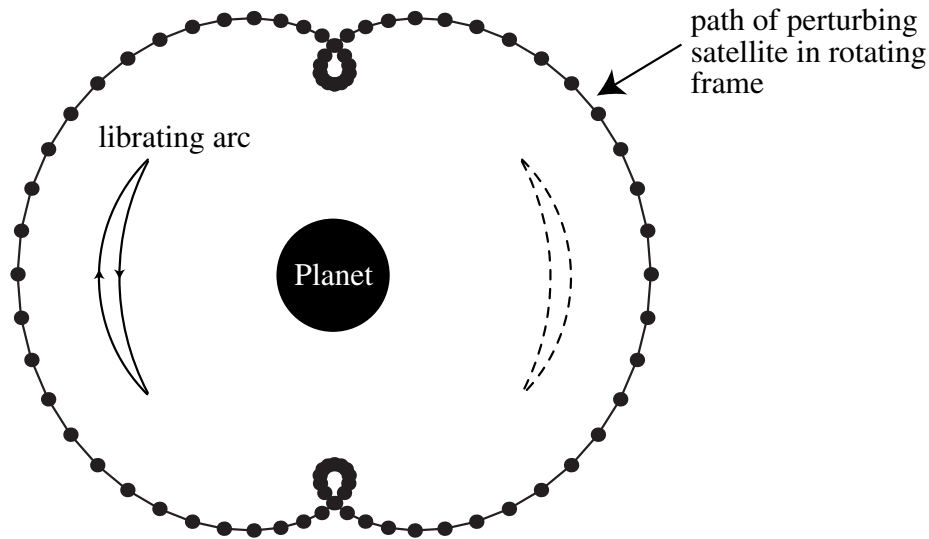
Fig. 10.7. The geometry of a 3:2 ($j = 3, m = 2, k = 1, p = 0$) corotation resonance for the case when $e' = 0.25$. In a frame corotating with the pattern speed of the perturbing satellite, $\Omega_p = n' + \kappa'/2$, there are two equilibrium points at this resonance. A ring particle close to one of these points will librate about a longitude that is stationary in the rotating frame (solid curve). Libration is also possible about the other equilibrium point (dashed curve).

argument 4D1.2 with $j = 3$. Taking the largest term in our previous expression for the maximum change in semi-major axis in a resonant libration (Eq. (8.58)) the width, W_{cr}, of a general corotation resonance can be written as

$$W_{\mathrm{cr}} = 8 \left(\frac{a \, |\mathcal{R}|}{3 \mathcal{G} m_{\mathrm{p}}} \right)^{\frac{1}{2}} a, \tag{10.10}$$

which agrees with the expressions given by Goldreich & Tremaine (1981) and Dermott (1984).

A feature associated with the Mimas 2:1 corotation resonance has been observed in Saturn's rings (Molnar & Dunn 1995). Corotation resonances have also been invoked to explain damping of eccentricities in narrow rings (Goldreich & Tremaine 1981) and the mutual repulsion of rings and satellites (Goldreich & Tremaine 1980).

Note that although we have formulated these expressions for the case where the satellite is an external perturber, the theory can still be applied to the case where the satellite orbits interior to the ring, provided we make minor changes in notation. As we shall see, an external corotation resonance is thought to be involved in the azimuthal confinement of the arcs in Neptune's Adams ring (see Sect. 10.8).

10.3.2 Perturbations in Eccentricity and Lindblad Resonances

A Lindblad resonance occurs when the pattern speed of the perturbing potential matches the radial frequency of the particle. In this case

$$m(n - \Omega_p) = \pm\kappa, \tag{10.11}$$

where the upper and lower signs correspond to the inner (ILR) and outer (OLR) Lindblad resonance respectively. The use of $\pm$ permits us to consider a ring particle that is orbiting inside or outside the orbit of the perturbing satellite. The resonance condition can also be written as

$$(m \mp 1)n \pm \dot{\varpi} - m\Omega_p = 0 \tag{10.12}$$

or

$$(m + k + p)n' - (m \mp 1)n - k\dot{\varpi}' \mp \dot{\varpi} - p\dot{\Omega}' = 0. \tag{10.13}$$

In terms of the resonant angle, φ_{Lr}, we have

$$\varphi_{Lr} = (m + k + p)\lambda' - (m \mp 1)\lambda - k\varpi' \mp \varpi - p\Omega'. \tag{10.14}$$

Using our standard notation we can write this as

$$\varphi_{Lr} = j\lambda' + (k + p \pm 1 - j)\lambda - k\varpi' \mp \varpi - p\Omega', \tag{10.15}$$

where, as before, $j = m + k + p$. Note that this is a resonant argument of order $|k + p \pm 1|$. Also, because the sum of the coefficients of Ω and Ω' must be even, p has to be even for all Lindblad resonances. To lowest order the term associated with φ_{Lr} is $\mathcal{O}(ee'^{|k|}I'^{|p|})$.

To help understand the mechanism of a Lindblad resonance we introduce the concept of a *streamline*, whereby we consider the motion of a collection of particles with the same semi-major axis and eccentricity. To lowest order in e the equation of an ellipse can be written as

$$r = a[1 - e\cos(\theta - \varpi)], \tag{10.16}$$

where θ is the true longitude. However, we know that $\dot{\theta} = n$ and $\dot{\varpi} = n - \kappa$. Therefore we can write the condition given in Eq. (10.11) as

$$m\frac{d}{dt}(\theta - \Omega_p t) = \pm\frac{d}{dt}(\theta - \varpi). \tag{10.17}$$

Integration of this equation shows that for a given semi-major axis and eccentricity the longitude, $\theta_c = \theta - \Omega_p t$, of the particles in a frame corotating with the pattern speed is given by

$$m\theta_c = \theta - \varpi + \text{constant}. \tag{10.18}$$

Hence the paths, or streamlines, are described by the equation

$$r = a\left[1 - e\cos\left(m\theta_c - \text{constant}\right)\right]. \tag{10.19}$$

The resulting streamlines for the cases $m = 0$ (a circle), $m = 1$ (a keplerian ellipse), $m = 2$ (a centred ellipse), and $m = 7$ (a seven-lobed curve) are shown in Fig. 10.8. In each case we have chosen the phase constant to be zero. Note that in the case of a keplerian ellipse, Fig. 10.8b, the path looks circular. This is because, to $\mathcal{O}(e)$, a keplerian ellipse is simply a circle displaced from its centre (see Eq. (2.101) and the discussion in Sect. 2.6). It is clear that the streamlines always produce an m-lobed pattern. Note the similarity with the paths in the rotating frame for interior first-order resonances shown in Fig. 8.3a. Because the Lindblad resonance involves only the first power of the eccentricity of the ring particle a streamline never intersects itself.

When discussing sharp edges near a discrete resonance in planetary rings it is important to define the physical width of a Lindblad resonance. The effect of the Lindblad resonance is to induce a forced eccentricity on the ring particles such that, at a given semi-major axis, the particles move in streamline motion. We have already noted that the resulting pattern in the rotating frame is a wavy, m-lobed ring. The size of the forced eccentricity will decrease as the distance from the exact resonance increases, with a phase change of $180°$ on opposite sides of the resonance. This phenomenon was illustrated in Fig. 8.11. The width of the resonance is determined by the separation from the exact resonance such that the value of the forced eccentricity is just sufficient for the outer streamline to intersect the inner one. The mechanism is discussed by Porco & Nicholson (1987). The resulting paths are illustrated in Fig. 10.9 for the case of the 7:6 Lindblad resonance with $k = p = 0$ and hence $\Omega_p = n'$.

In Sect. 8.8.1 we discussed the location of the equilibrium points for the case of large values of $\bar{\delta}$, corresponding to motion far from the resonance (see Fig. 8.11). There we noted that for the e resonance the relevant part of the disturbing function is

$$\mathcal{R} = \frac{\mathcal{G}m'}{a'} f_d(\alpha) e \cos \varphi_{Lr}, \tag{10.20}$$

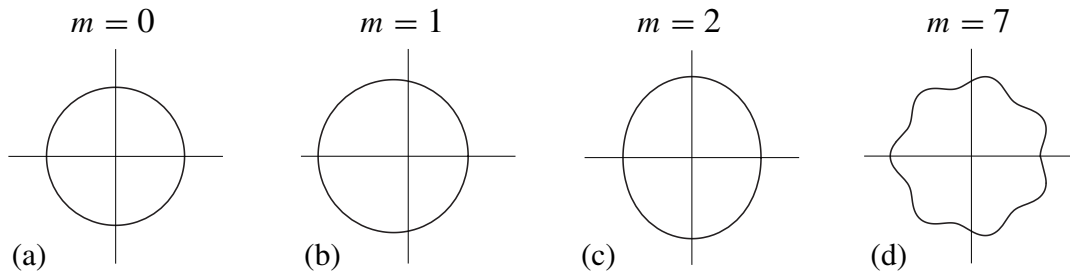| $m = 0$ | $m = 1$ | $m = 2$ | $m = 7$ |
| (a) | (b) | (c) | (d) |

Fig. 10.8. Streamline paths obtained for (a) $m = 0$, $\Omega_p = k\kappa'$, (b) $m = 1$, $\Omega_p = n' + k\kappa'$, (c) $m = 2$, $\Omega_p = n' + (k/2)\kappa'$, and (d) $m = 7$, $\Omega_p = n' + (k/7)\kappa'$ using the same semi-major axis and $e = 0.08$ in (a), (c), and (d) and $e = 0.2$ in (b).
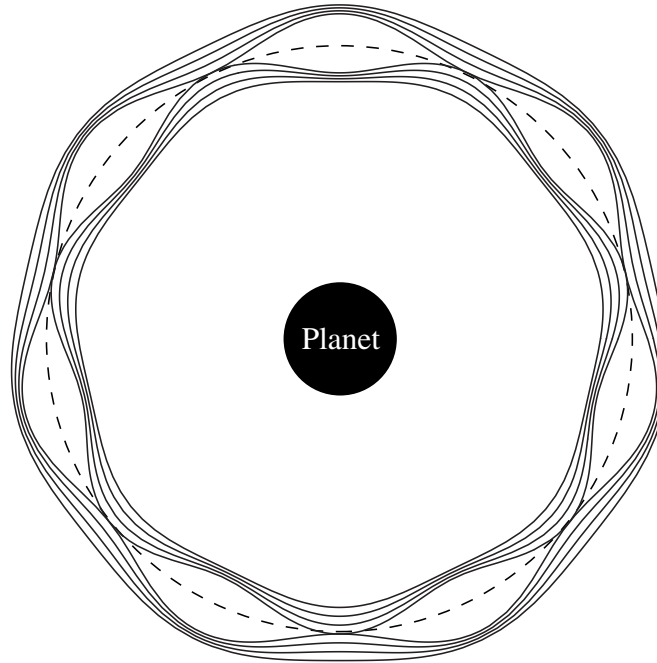
Fig. 10.9. A schematic diagram illustrating the streamlines for the 7:6 Lindblad reso-
nance ($j = 7$, $m = 7$, $k = 0$, $p = 0$) with $\Omega_\mathrm{p} = n'$. The curves denote the streamlines
of particle orbits on either side of exact resonance, denoted by the dashed circle. The
amplitude of each streamline is a linear function of the forced eccentricity, and the width
of the resonance is determined by the distance from the resonance at which streamlines
on opposite sides just touch.

where $\varphi_\mathrm{Lr} = j\lambda' - (j - 1)\lambda - \varpi$ and $f_\mathrm{d} = (1/2)\left[-2j - \alpha D\right] b_{1/2}^{(j)}$ (see Table 8.1).
This is the $k = p = 0$ Lindblad resonance in our new terminology. The location
of the equilibrium point gives the value of the scaled forced eccentricity and
is simply $2/\bar{\delta}$, where $\bar{\delta}$ is a measure of the proximity to resonance. Using the
scaling relation given in Eq. (8.132) and the definitions of $\bar{\alpha}$, $\bar{\beta}$, and $\bar{\epsilon}$ given
in Eqs. (8.103)–(8.105) for first-order resonances, we can write the resulting
expression for the forced eccentricity as

$$e_\mathrm{f} = \left| \frac{n\alpha(m'/m_\mathrm{p}) f_\mathrm{d}}{[jn' - (j - 1)n]} \right|. \tag{10.21}$$

If we write $a = a_\mathrm{res} + \Delta a$ (where $\Delta a \ll a_\mathrm{res}$) for the semi-major axis of the
particle we can make use of Kepler's third law and a series expansion in $\Delta a/a_\mathrm{res}$
to write the amplitude of the resulting forced wave as

$$ae_\mathrm{f} = \frac{2\alpha a^2 (m'/m_\mathrm{p}) |f_\mathrm{d}|}{3(j - 1) |a - a_\mathrm{res}|} \tag{10.22}$$

for the case $k = p = 0$. For a critical value of the semi-major axis, a_crit, the
amplitude of the ring wave equals the separation in semi-major axis from the
exact resonance. For this value the full width of the $k = p = 0$ Lindblad

resonance is given by

$$W_{\mathrm{Lr},0} = 4a \left[\frac{2\alpha(m'/m_{\mathrm{p}})|f_{\mathrm{d}}|}{3(j-1)} \right]^{\frac{1}{2}}. \tag{10.23}$$

The values of $\alpha = a/a'$ and the corresponding Laplace coefficients in the definition of f_{d} can be calculated for any particular value of j. Figure 10.10 shows a plot of the variation of the quantity $2\alpha f_{\mathrm{d}}/(j-1)$ as a function of j for the resonances 2:1 to 50:49 inclusive (corresponding to $j=2$ to $j=50$). This shows that provided j is sufficiently large, $2\alpha f_{\mathrm{d}}/(j-1) \approx 1.6$ and hence, from our expression for $W_{\mathrm{Lr},0}$, we can write

$$W_{\mathrm{Lr},0} \approx 2.9(m'/m_{\mathrm{p}})^{\frac{1}{2}}a. \tag{10.24}$$

This gives us a useful expression for the width of the general $k=p=0$ ILR. Note that this width is approximately the same for all first-order resonances.

Lindblad resonances are thought to play a key role in the confinement of narrow rings. For example, observations have shown that the outer and inner edges of the ϵ ring of Uranus are located at the Ophelia 14:13 ILR and the Cordelia 24:25 OLR. It is also known that the existence of Lindblad resonances with satellites such as Mimas, Janus, Pandora, and Prometheus in Saturn's rings gives rise to density waves in the immediate vicinity of the resonance. This is discussed in Sect. 10.4 below. The theory given above for first-order resonances
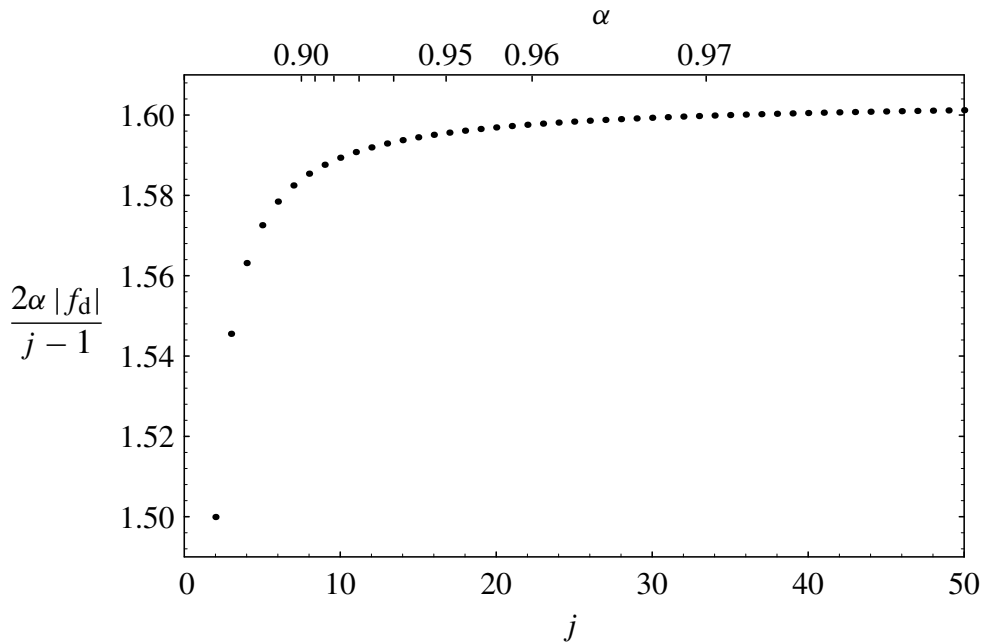

Fig. 10.10. A plot of $2\alpha|f_{\mathrm{d}}|/(j-1)$ as a function of j (lower scale) and α (upper scale) for all the $j:j-1$ ILRs with $k=p=0$ from the 2:1 to the 50:49.

can easily be extended to handle higher order resonances using the results given in Sect. 8.8.

10.3.3 Perturbations in Inclination and Vertical Resonances

A vertical resonance occurs where the pattern speed of the perturbing potential matches the vertical frequency of the particle. In this case

$$m(n - \Omega_p) = \pm \nu, \tag{10.25}$$

where the upper and lower signs correspond to the inner (IVR) and outer (OVR) vertical resonances respectively. The resonance condition can also be written as

$$(m \mp 1)n \pm \dot{\Omega} - m\Omega_p = 0 \tag{10.26}$$

or

$$(m + k + p)n' - (m \mp 1)n - k\dot{\varpi}' \mp \dot{\Omega} - p\dot{\Omega}' = 0. \tag{10.27}$$

In terms of the resonant angle, φ_{vr}, we have

$$\varphi_{vr} = (m + k + p)\lambda' - (m \mp 1)\lambda - k\varpi' \mp \Omega - p\Omega'. \tag{10.28}$$

Using our standard notation we can write this as

$$\varphi_{vr} = j\lambda' + (k + p \pm 1 - j)\lambda - k\varpi' - p\Omega' \mp \Omega, \tag{10.29}$$

where, as before, $j = m + k + p$. Note that this is a resonant argument of order $|k + p \pm 1|$. Also, since the sum of the coefficients of Ω and Ω' must be even, p has to be odd for all vertical resonances. The lowest order term associated with φ_{vr} is $\mathcal{O}(e'^{|k|}II'^{|p|})$.

Consider the case of the strong $k = 0$, $p = 1$ vertical resonance. This is equivalent to the II' resonance discussed in Sect. 8.8.4. The relevant part of the disturbing function is

$$\mathcal{R} = \frac{\mathcal{G}m'}{a'} f_d(\alpha)ss' \cos \varphi_{vr}, \tag{10.30}$$

where $s = \sin \frac{1}{2}I$, $s' = \sin \frac{1}{2}I'$, $\varphi_{vr} = j\lambda' - (j - 2)\lambda - \Omega' - \Omega$, and $f_d = -\alpha b_{3/2}^{(j-1)}$ (see Table 8.1). Just as the Lindblad resonance is due to a forced eccentricity, so the vertical resonance is due to a forced inclination. There is also a phase shift of 180° in the longitude of ascending node on either side of the vertical resonance, as in the case of the longitude of pericentre in the Lindblad resonance. The location of the equilibrium point as a function of $\bar{\delta}$ (the distance from exact resonance), and hence the value of the scaled forced inclination, is given by Eq. (8.187). When $\bar{\delta}$ is large this gives a value of $2c/\bar{\delta}$. Using the standard scaling relationships gives a forced inclination of

$$I_f = \left| \frac{n\alpha(m'/m_p)\sin I' f_d}{4[jn' - (j - 1)n]} \right|. \tag{10.31}$$

The resulting amplitude of the forced vertical wave can be written as

$$aI_\mathrm{f} = \frac{\alpha a^2 (m'/m_\mathrm{p}) \sin I' |f_\mathrm{d}|}{6(j-2)|a - a_\mathrm{res}|}. \tag{10.32}$$

Although it is tempting to use the analogy with the Lindblad resonance to calculate an expression for the width of a vertical resonance, in reality the concept is meaningless partly because adjacent streamlines never intersect.

An OVR with Galatea is thought to play a role in the radial confinement of the Adams ring of Neptune. It is also known that the existence of IVRs with Mimas ($I' \approx 1.5°$) in Saturn's rings gives rise to bending waves in regions immediately interior to the resonance. This is discussed in Sect. 10.4.

10.3.4 Locations of Resonances

Using Kepler's third law, the approximate semi-major axis of an internal $p+q : p$ resonance is given by $a = [p/(p+q)]^{2/3} a'$, where a' is the semi-major axis of the perturbing object. However, as we have seen in Chapter 8, the semi-major axis of the *exact* resonance depends on the particular resonant argument under consideration. Consider a general resonant argument of the form

$$\varphi = j_1 \lambda' + j_2 \lambda + j_3 \varpi' + j_4 \varpi + j_5 \Omega' + j_6 \Omega. \tag{10.33}$$

This argument is associated with the general $|j_1| : |j_2|$ resonance. If we ignore the variation of the mean longitude at epoch, the location of the exact resonance is given by the semi-major axis that satisfies the equation

$$j_1 n' + j_2 n + j_3 \dot\varpi' + j_4 \dot\varpi + j_5 \dot\Omega' + j_6 \dot\Omega = 0. \tag{10.34}$$

In the case of resonances with planets (e.g., jovian resonances in the asteroid belt) the dominant contribution to the $\dot\varpi$ and $\dot\Omega$ terms comes from the secular perturbations from the perturber itself and tends to be small. This means that the locations of the exact resonances corresponding to the various resonant arguments are all close to one another. However, in the case of resonances with planetary satellites the effect of the planet's oblateness invariably dominates the motion of the perturbed object's pericentre and node, especially in regions close to the planet. This leads to the phenomenon of resonance splitting discussed in Sect. 8.11, whereby the locations of the exact resonances at a given commensurability will be spread out. Furthermore, because $\dot\varpi$ and $\dot\Omega$ are approximately equal in magnitude but opposite in sign (ϖ precesses and Ω regresses), those resonances involving only the pericentres or only the nodes will be equidistant (outside and inside respectively) from the location of the nominal resonance given by $a = |j_2/j_1|^{2/3} a'$, or, more precisely, $n = |j_1/j_2| n'$. Unfortunately n, $\dot\varpi$, and $\dot\Omega$ depend on a in a nonlinear manner and so a numerical method is required to find the location of the exact resonance for a given argument.

Table 10.1. The type, classification, and parameters for the Mimas 3:1, 2:1, 4:2, 5:3, and 8:5 resonances in Saturn's rings.

Resonant angle, φ	Type	Class.	j	m	k	p	a (km)	Feature
$3\lambda' - \lambda - 2\Omega$	I^2	—	3	—	—	—	88,029	
$3\lambda' - \lambda - \Omega' - \Omega$	II'	IVR	3	2	0	1	88,705	•
$3\lambda' - \lambda - 2\Omega'$	I'^2	CIR	3	1	0	2	89,356	
$3\lambda' - \lambda - 2\varpi'$	e'^2	CER	3	1	2	0	89,562	
$3\lambda' - \lambda - \varpi' - \varpi$	ee'	ILR	3	2	1	0	90,193	•
$3\lambda' - \lambda - 2\varpi$	e^2	—	3	—	—	—	90,802	
$4\lambda' - 2\lambda - 2\Omega$	I^2	—	4	—	—	—	116,512	
$4\lambda' - 2\lambda - \Omega' - \Omega$	II'	IVR	4	3	0	1	116,725	
$4\lambda' - 2\lambda - 2\Omega'$	I'^2	CIR	4	2	0	2	116,935	
$4\lambda' - 2\lambda - 2\varpi'$	e'^2	CER	4	2	2	0	117,138	
$2\lambda' - \lambda - \varpi'$	e'	CER	2	1	1	0	117,138	•
$4\lambda' - 2\lambda - \varpi' - \varpi$	ee'	ILR	4	3	1	0	117,346	•
$4\lambda' - 2\lambda - 2\varpi$	e^2	—	4	—	—	—	117,552	
$2\lambda' - \lambda - \varpi$	e	ILR	2	2	0	0	117,552	•
$5\lambda' - 3\lambda - 2\Omega$	I^2	—	5	—	—	—	131,793	
$5\lambda' - 3\lambda - \Omega' - \Omega$	II'	IVR	5	4	0	1	131,900	•
$5\lambda' - 3\lambda - 2\Omega'$	I'^2	CIR	5	3	0	2	132,007	
$5\lambda' - 3\lambda - 2\varpi'$	e'^2	CER	5	3	2	0	132,191	
$5\lambda' - 3\lambda - \varpi' - \varpi$	ee'	ILR	5	4	1	0	132,298	•
$5\lambda' - 3\lambda - 2\varpi$	e^2	—	5	—	—	—	132,404	
$8\lambda' - 5\lambda - \varpi' - 2\Omega$	$e'I^2$	—	8	—	—	—	135,582	
$8\lambda' - 5\lambda - \varpi' - \Omega' - \Omega$	$e'II'$	IVR	8	6	1	1	135,642	•
$8\lambda' - 5\lambda - \varpi - 2\Omega$	eI'^2	—	8	—	—	—	135,642	
$8\lambda' - 5\lambda - \varpi' - 2\Omega'$	$e'I'^2$	—	8	—	—	—	135,701	
$8\lambda' - 5\lambda - \varpi - \Omega' - \Omega$	eII'	—	8	—	—	—	135,702	
$8\lambda' - 5\lambda - \varpi - 2\Omega'$	eI'^2	ILR	8	6	0	2	135,761	
$8\lambda' - 5\lambda - 3\varpi'$	e'^3	CER	8	5	3	0	135,820	
$8\lambda' - 5\lambda - 2\varpi' - \varpi$	ee'^2	ILR	8	6	2	0	135,879	•
$8\lambda' - 5\lambda - \varpi' - 2\varpi$	e^2e'	—	8	—	—	—	135,938	
$8\lambda' - 5\lambda - 3\varpi$	e^3	—	8	—	—	—	135,998	

Notes: φ is the resonant angle. In the classification column ILR, IVR, CER, and CIR denote inner Lindblad resonance, inner vertical resonance, corotation eccentricity resonance, and corotation inclination resonance respectively. The "•" symbol in the final column denotes that there is an associated feature in Saturn's rings at this location.

As an example, Table 10.1 shows the results of such calculations for a selection of 3:1, 2:1, 4:2, 5:3, and 8:5 Mimas resonances that lie in Saturn's rings. In order to derive the locations of the resonances we have taken the mean motion, perichrone rate, and node rate of Mimas to be $381.9945°\mathrm{d}^{-1}$, $1.0008°\mathrm{d}^{-1}$, and $-0.9995°\mathrm{d}^{-1}$ respectively (Harper & Taylor 1993). We have taken $\mathcal{G}m_\mathrm{p}$ for Saturn to be $3.79312 \times 10^7 \ \mathrm{km^3 s^{-2}}$ and also included secular perturbations from Mimas in the calculation, although the latter are negligible. In the table we indicate the "type" of the resonance, using the terminology adopted in Chapter 8, as well as the "classification" of the resonance (denoted by "Class" in the table) using the terminology of ring dynamics. The effect of the oblateness causes the resonances at a given commensurability to be spread out in semi-major axis. Note that two pairs of resonances (the e and e^2 resonances, and the e' and e'^2 resonances) have the same location because the respective 4:2 arguments are simply twice the 2:1 arguments and therefore they have the same equation corresponding to exact resonance. Note that a number of resonances are not classified under the terminology of ring dynamics.

10.4 Density Waves and Bending Waves

The effect of a satellite resonance in a ring of sufficiently high surface density is to introduce an azimuthal variation in the gravitational potential. For example, we have already seen that a $j : j - 1$ inner Lindblad resonance gives rise to a j-lobed pattern in the streamlines of particle paths in the vicinity of the resonance (see Fig. 10.9). In general, it is the value of m rather than j that determines the number of lobes, although for first-order ILRs, $j = m$ (see Table 10.1). Beyond the resonance width, as the distance from exact resonance increases, each streamline shifts in azimuth but the whole pattern remains stationary in the rotating reference frame. This gives rise to a spiral pattern with m spiral arms (see Fig. 10.11), even though each individual particle remains on a keplerian ellipse. The pattern is called a *spiral density wave*. Because the resulting gravitational potential varies with the same period as that due to the satellite, the spiral pattern is reinforced. In practice the spiral is very tightly wound, but a radial profile would always show the characteristic decrease in wavelength (the distance from peak to peak or trough to trough) with increasing distance from exact resonance.

There is an equivalent phenomenon due to vertical resonances. In this case the forced oscillations are in the vertical rather than the radial direction (i.e., there is a forced inclination) and the systematic shifts in azimuth lead to the formation of *spiral bending waves*. For an inner vertical resonance the result is trailing bending waves that propagate inwards from the exact resonance (see Fig. 10.12).

The basic theory of density waves was originally developed to explain the spiral structure of some galaxies, but Goldreich & Tremaine (1978b) adapted it to explain the formation of the Cassini division in Saturn's rings. Since then
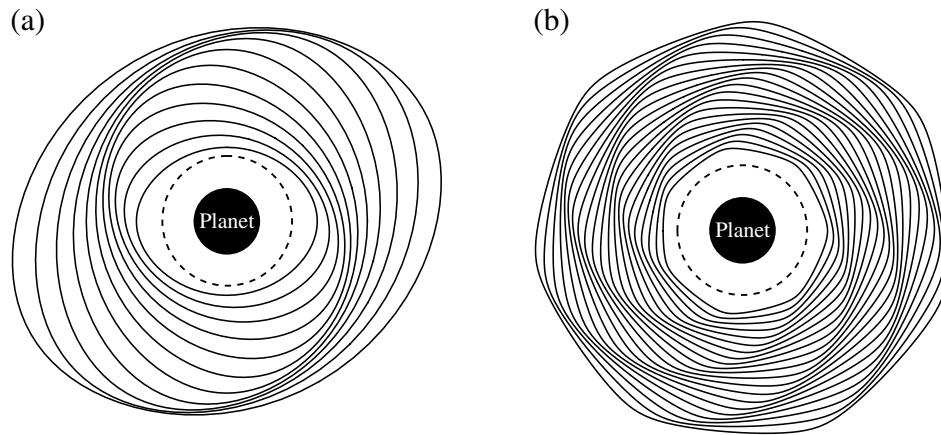
(a)

(b)

Fig. 10.11. Schematic diagrams of the coplanar particle paths that give rise to trailing spiral density waves near a resonance with an exterior satellite. (a) The two-armed spiral density wave associated with the 2:1 ($m = 2$) inner Lindblad resonance. (b) The seven-armed density wave associated with the 7:6 ($m = 7$) inner Lindblad resonances. The pattern rotates with the angular velocity of the satellite and propagates outwards from the exact resonance (denoted by the dashed circle).

significant advances in the theory have been made (see, for example, the review by Shu (1984) and the work of Rosen (1989).

Spiral density and bending waves have now been detected at many locations in Saturn's rings (Holberg et al. 1982, Lane et al. 1982, Shu et al. 1983). In Table 10.1 we list some examples of Mimas resonances in Saturn's rings. Because Mimas has an appreciable inclination (1.5°) its vertical resonances are comparable in strength to its Lindblad resonances. When strong resonances occur in rings of sufficient surface density it is possible to see the effects of resonance. Figure 10.13 shows part of a *Voyager 2* image of Saturn's A ring in the vicinity

(a)

(b)
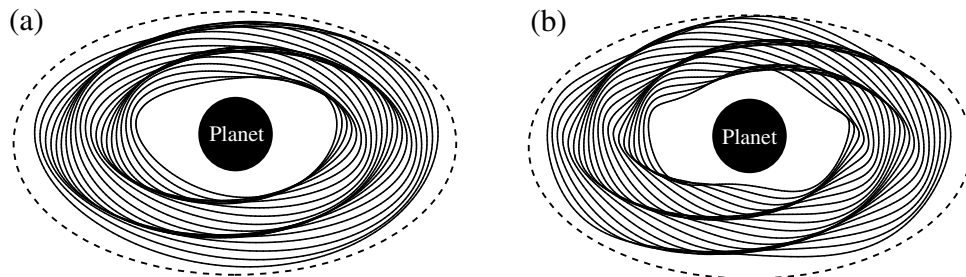
Fig. 10.12. Schematic diagrams showing an oblique view of the three-dimensional particle paths that give rise to trailing spiral bending waves near a resonance with an exterior satellite. (a) The two-armed spiral bending wave associated with the 3:1 ($m = 2$) inner vertical resonance. (b) The four-armed bending wave associated with the 5:3 ($m = 4$) inner vertical resonances. The pattern rotates with the angular velocity of the satellite and propagates inwards from the exact resonance (denoted by the dashed curve).

of the 5:3 Mimas commensurability and the accompanying occultation profile
from the *Voyager* PPS experiment. Here the location of the ILR lies 398 km
outside the location of the IVR (see Table 10.1). The spiral density wave due to
the 5:3 ILR is at the left (larger radius) of the image and is propagating outwards
with the characteristic decrease in wavelength with increasing distance from the
resonance. At the right of the image is the spiral bending wave due to the 5:3
IVR propagating inwards. The additional radial feature just interior to the 5:3
density wave is due to an ILR with Prometheus. Note that whereas a density
wave gives rise to density enhancements in the ring plane, the bending wave
produces actual "corrugations", which take particles out of the ring plane. This
accounts for the difference in physical appearance of the two spiral waves shown
in Fig. 10.13. The more extreme contrast visible of the bending wave was caused
by the effect of alternate brightness and shadow due to the vertically displaced
ring material being illuminated by the Sun, which was $8°$ above the ring plane
at the time the image was taken.

Further examples of density and bending waves are shown in Fig. 10.5. Al-
though there is insufficient radial resolution in the image to detect individual
peaks and troughs, the effects of the density waves due to Prometheus and
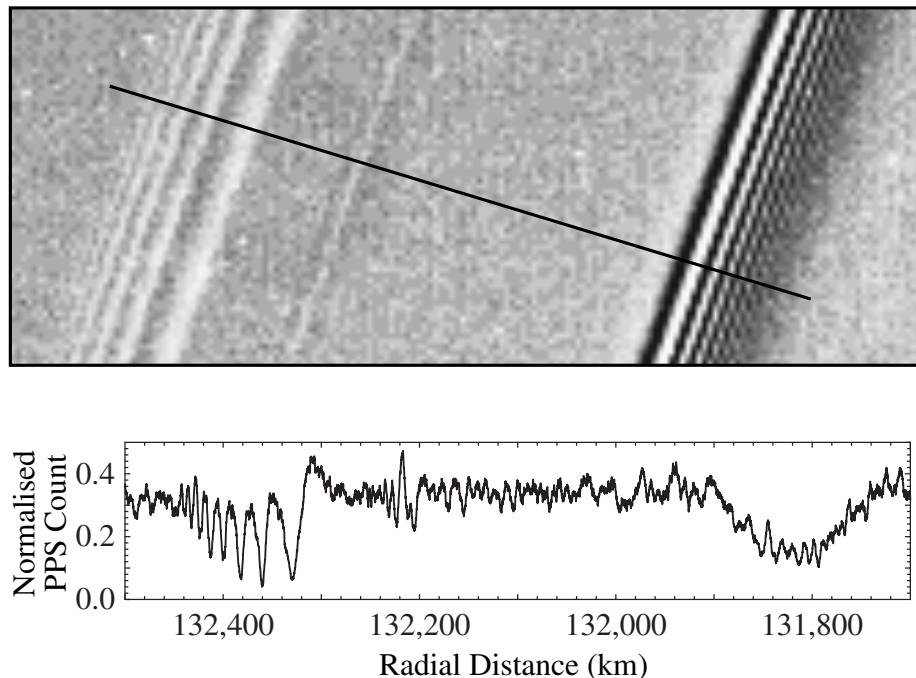
Fig. 10.13. *Voyager* image and associated photopolarimeter (PPS) occultation profile of
spiral density waves (left) and spiral bending waves (right) produced by the 5:3 Mimas
resonance in Saturn's A ring. The density and bending waves propagate outwards
and inwards respectively from the locations of exact resonance. *(Image courtesy of
NASA/JPL. PPS data courtesy of NASA PDS Rings node.)*

Pandora ILRs near the outer part of Saturn's A ring are clearly visible. Furthermore, the density and bending waves associated with the 8:5 Mimas commensurability are also evident.

Appendix A
Solar System Data

And he that calls on thee, let him bring forth
Eternal numbers to outlive long date.

William Shakespeare, *Sonnet XXXVIII*

A.5 Planets, Satellites, and Rings

In Table A.4 we list the physical properties of each of the planets. Data are taken
from Yoder (1995). The quoted value of R in Table A.4 is the reference radius
used in the determination of J_2 and J_4. This is the value of the planetary radius
to be used in calculations of precession due to oblateness.

In Tables A.5–A.15 we list data relating to the satellites and, where appropri-
ate, ring systems of each planet. In these tables a is the semi-major axis, T is the
sidereal orbital period (with a minus sign denoting retrograde orbital motion), e
is the eccentricity, I is the inclination of the satellite's orbit to the planet's equator
(except where noted), $\langle R \rangle$ is the mean radius in km (with a preceding $*$ denoting

that it is an irregularly shaped body), and m is the mass of the satellite. Values of e and I preceded by the letter "f" indicate that the value is a forced quantity, usually due to a resonance. Values of I preceded by the letter "e" indicate that the inclination is with respect to the ecliptic. The letter "c" after a satellite name denotes that it is a coorbital object. For rings τ denotes the optical depth of the ring.

Most of the data are taken from the tables contained in Yoder (1995) with minor corrections. Additional sources of data are noted in the table footnotes.

Table A.4. Physical properties of the planets.

Planet	m_p (10^{24}kg)	R (km)	T_{rot} (h)	$\langle\rho\rangle$	ϵ (°)	J_2	J_4
Mercury	0.3302	2,440	1047.51	5.427	~ 0.1	60	
Venus	4.8685	6,052	−5832.444	5.204	177.3	4	2
Earth	5.9736	6,378	23.93419	5.515	23.45	1083	−2
Mars	0.64185	3,394	24.622962	3.933	25.19	1960	−19
Jupiter	1898.6	71,398	9.92425	1.326	3.12	14736	−587
Saturn	568.46	60,330	10.65622	0.6873	26.73	16298	−915
Uranus	86.832	26,200	−17.24	1.318	97.86	3343	−29
Neptune	102.43	25,225	16.11	1.638	29.56	3411	−35
Pluto	0.0127	1,137	−153.29	2.06	112.52		

Notes: m_p is the mass of the planet, R is its reference radius, T_{rot} is the sidereal rotational period (referred to a fixed frame of reference) with a minus sign denoting retrograde rotation, $\langle\rho\rangle$ is the mean density (in g cm^{-3}), ϵ is the obliquity, and J_2 ($\times10^{-6}$) and J_4 ($\times10^{-6}$) denote the first two even gravitational harmonics.

Table A.5. The satellite of Earth.

Satellite	a (km)	T (d)	e	I (°)	$\langle R\rangle$	m (10^{20}kg)
Moon	384,400	27.321661	0.054900	5.15	1737.53	734.9

Table A.6. The satellites of Mars.

Satellite	a (km)	T (d)	e	I (°)	$\langle R\rangle$	m (10^{15}kg)
Phobos	9,377.2	0.318910	0.0151	1.082	*11	10.8
Deimos	23,463.2	1.262441	0.00033	1.791	*6	1.8

Table A.7. The satellites of Jupiter.

Satellite	a (km)	T (d)	e	I (°)	$\langle R \rangle$	m (10^{20}kg)
Metis	127,979	0.294780	< 0.004	~ 0	20	
Adrastea	128,980	0.29826	~ 0	~ 0	10	
Amalthea	181,300	0.498179	0.003	0.40	*86	
Thebe	221,900	0.6745	0.015	0.8	50	
Io	421,600	1.769138	[f]0.0041	0.040	1,821	893.3
Europa	670,900	3.551810	[f]0.0101	0.470	1,565	479.7
Ganymede	1,070,000	7.154553	[f]0.0015	0.195	2,634	1482
Callisto	1,883,000	16.689018	0.007	0.281	2,403	1076
Leda	11,094,000	238.72	0.148	27	5	
Himalia	11,480,000	250.5662	0.163	25	85	
Lysithea	11,720,000	259.22	0.107	29	12	
Elara	11,737,000	259.6528	0.207	28	40	
Ananke	21,200,000	−631	0.169	147	10	
Carme	22,600,000	−692	0.207	163	15	
Pasiphae	23,500,000	−735	0.378	148	18	
Sinope	23,700,000	−758	0.275	153	14	

Note: The semi-major axis of Metis is taken from Nicholson & Matthews (1991).

Table A.8. The ring system of Jupiter.

Ring	Inner Edge (km)	Outer Edge (km)	τ
halo	89,400	123,000	3×10^{-6}
main	123,000	128,940	5×10^{-6}
gossamer	128,940	242,000	1×10^{-7}

Table A.9. The satellites of Saturn.

Satellite	a (km)	T (d)	e	I (°)	$\langle R \rangle$	m (10^{20}kg)
Pan	133,583	0.5750	~ 0	~ 0	10	
Atlas	137,640	0.6019	~ 0	~ 0	*16	
Prometheus	139,350	0.612986	0.0024	0.0	*50	0.0014
Pandora	141,700	0.628804	0.0042	0.0	*42	0.0013
Epimetheus[c]	151,422	0.694590	0.009	0.34	*59	0.0055
Janus[c]	151,472	0.694590	0.007	0.14	*89	0.0198
Mimas	185,520	0.9424218	0.0202	[f]1.53	199	0.385
Enceladus	238,020	1.370218	[f]0.0045	0.02	249	0.73
Tethys	294,660	1.887802	0.0000	[f]1.09	530	6.22
Telesto[c]	294,660	1.887802	~ 0	~ 0	*11	
Calypso[c]	294,660	1.887802	~ 0	~ 0	*10	
Dione	377,400	2.736915	[f]0.0022	0.02	560	10.52
Helene[c]	377,400	2.736915	0.005	0.2	*16	
Rhea	527,040	4.517500	[f]0.0010	0.35	764	23.1
Titan	1,221,850	15.945421	0.0292	0.33	2,575	1345.5
Hyperion	1,481,100	21.276609	[f]0.1042	0.43	*143	
Iapetus	3,561,300	79.330183	0.0283	7.52	718	15.9
Phoebe	12,952,000	−550.48	0.163	175.3	110	

Table A.10. The ring system of Saturn.

Ring	a (km)	W (km)	e	τ
D (inner edge)	66,900	7,758		
C (inner edge)	74,658	17,317		0.05–0.35
Titan ringlet	77,871	25	0.00026	
Maxwell ringlet	87,491	64	0.00034	
1.470 R_S ringlet	88,716	16	0.000023	
1.495 R_S ringlet	90,171	61	0.000031	
B (inner edge)	91,975	25,532		0.4–2.5
B (outer edge)	117,507			
Huygens ringlet	117,825	360	0.00040	
A (inner edge)	122,340	14,440		0.4–1.0
Encke ringlet	133,589	20		
A (outer edge)	136,780			
F (core)	140,219	50	0.0028	0.1
G (inner edge)	166,000	7,200		1×10^{-6}
E (inner edge)	180,000	300,000		1.5×10^{-5}

Note: Additional data are from Porco & Nicholson (1987) and Murray et al. (1997).

Table A.11. The satellites of Uranus.

Satellite	a (km)	T (d)	e	I (°)	⟨R⟩	m (10^{20}kg)
Cordelia	49,752	0.3350331	0.000	0.1	13	
Ophelia	53,764	0.3764089	0.010	0.1	16	
Bianca	59,165	0.4345772	0.001	0.2	22	
Cressida	61,767	0.4635700	0.000	0.0	33	
Desdemona	62,659	0.4736510	0.000	0.2	29	
Juliet	64,358	0.4930660	0.001	0.1	42	
Portia	66,097	0.5131958	0.000	0.1	55	
Rosalind	69,927	0.5584589	0.000	0.3	29	
Belinda	75,255	0.6235248	0.000	0.0	34	
Puck	86,004	0.7618321	0.000	0.3	77	
Miranda	129,800	1.413	0.0027	4.22	*235	0.659
Ariel	191,200	2.520	0.0034	0.31	*579	13.53
Umbriel	266,000	4.144	0.0050	0.36	585	11.72
Titania	435,800	8.706	0.0022	0.10	789	35.27
Oberon	583,600	13.463	0.0008	0.10	761	30.14
Caliban	7,169,000	−580	0.0823	^{e}139.67	40	
Sycorax	12,213,000	−1289	0.5091	^{e}152.67	80	

Note: Data on Cordelia, Ophelia, Bianca, Cressida, Desdemona, Juliet, Portia, Rosalind, Belinda, and Puck are from Owen & Synnott (1987). Data on Caliban and Sycorax are from Marsden & Williams (1997).

Table A.12. The ring system of Uranus.

Ring	a (km)	W (km)	e	I (°)	τ
6	41,837	∼ 1.5	0.00101	0.062	∼ 0.3
5	42,234	∼ 2	0.00190	0.054	∼ 0.5
4	42,571	∼ 2.5	0.00106	0.032	∼ 0.3
α	44,718	4 → 10	0.00076	0.015	∼ 0.4
β	45,661	5 → 11	0.00044	0.005	∼ 0.3
η	47,176	1.6			≤ 0.4
γ	47,627	1 → 4	0.00109	0.000	≥ 1.5
δ	48,300	3 → 7	0.00004	0.001	∼ 0.5
λ	50,024	∼ 2	0.0	0.0	∼ 0.1
ε	51,149	20 → 96	0.00794	0.000	0.5–2.3

Note: Data are from French et al. (1991). Note that the δ and γ rings exhibit additional normal modes that affect their shape (see Sect. 10.5.4).

Table A.13. The satellites of Neptune.

Satellite	a (km)	T (d)	e	I (°)	$\langle R \rangle$	m (10^{20}kg)
Naiad	48,227	0.294396	0.000	4.74	29	
Thalassa	50,075	0.311485	0.000	0.21	40	
Despina	52,526	0.334655	0.000	0.07	74	
Galatea	61,953	0.428745	0.000	0.05	79	
Larissa	73,548	0.554654	0.000	0.20	*94	
Proteus	117,647	1.122315	0.000	0.55	*209	
Triton	354,760	−5.876854	0.0004	156.834	1353	215
Nereid	5,513,400	360.13619	0.7512	7.23	170	

Note: Data on Naiad, Thalassa, Despina, Galatea, Larissa, and Proteus are from Owen et al. (1991).

Table A.14. The ring system of Neptune.

Ring	a (km)	W (km)	τ
Galle	42,000	2,000	$\sim 1 \times 10^{-4}$
Le Verrier	53,200	<100	0.01
Lassell (inner edge)	53,200	4,000	$\sim 1 \times 10^{-4}$
Arago	57,200		
[unnamed]	61,953		
Adams	62,932.57	15	0.01–0.1

Note: Data are from Porco et al. (1995).

Table A.15. The satellite of Pluto.

Satellite	a (km)	T (d)	e	I (°)	$\langle R \rangle$	m (10^{20}kg)
Charon	19,636	6.387223	0.0076	96.163	593	15

Note: Orbital data are from Tholen & Buie (1997). Note that Charon's inclination is measured with respect to the mean equator and equinox of J2000.

A.6 Asteroids, Centaurs, Trans-Neptunian Objects, and Comets

Orbital and physical data given Tables A.16–A.18 are from the files maintained by Ted Bowell at *ftp://ftp.lowell.edu/pub/elgb/astorb.html*. The orbital data on the comets listed in Table A.19 were compiled from data maintained by JPL at *http://ssd.jpl.nasa.gov*.